

# **AQUARIUS SCATTEROMETER ALGORITHM THEORETICAL BASIS DOCUMENT**

Version 1

Simon Yueh, Alexander Fore, Adam Freedman, Mario J. Chaubell, Wenqing Tang,  
and Greg Neumann

**March 15, 2012**

 **JPL** Jet Propulsion Laboratory  
California Institute of Technology

**Contributors and Reviewers:**

<b>Name</b>	<b>Organization</b>
Fore, Alexander	Jet Propulsion Laboratory
Chaubell, Mario J.	Jet Propulsion Laboratory
Freedman, Adam	Jet Propulsion Laboratory
Neumann, Gregory	Jet Propulsion Laboratory
Tang, Wenqing	Jet Propulsion Laboratory
Yueh, Simon	Jet Propulsion Laboratory

Document Change Log

<b>Date</b>	Page Numbers	<b>Version</b>	<b>Changes/Comments</b>

## Table of Contents

1	SCOPE.....	1-1
2	APPLICABLE DOCUMENTS.....	2-2
3	INTRODUCTION.....	3-3
4	GEOMETRY AND GEO-LOCATION.....	4-4
4.1	Computation of Spacecraft Nadir Direction.....	4-4
4.2	Computation of Beam Bore-Sight Look Vector.....	4-4
4.3	Geolocation of Antenna Footprint on Earth.....	4-6
4.4	Computation of Incidence Angle and Azimuth Angle.....	4-7
4.5	Computation of Polarization Roll Angle.....	4-7
4.6	Computation of Beam Edge Points.....	4-8
5	RADIOMETRIC CALIBRATION.....	5-9
5.1	Calibration Equation.....	5-9
5.2	Look-up Table for K-factor.....	5-10
6	ANTENNA POLARIZATION AND FARADAY ROTATION CORRECTION.....	6-12
6.1	Antenna Polarization Correction.....	6-12
6.2	Faraday Rotation Angle Estimation.....	6-13
6.3	Faraday Rotation Correction.....	6-13
7	LAND AND SEA ICE FRACTIONS.....	7-14
8	RFI FLAG AND MITIGATION.....	8-16
8.1	Onboard RFI Detection.....	8-16
8.2	Ground-Based RFI Detection.....	8-17
8.3	RFI Flagging Results.....	8-18
9	GEOPHYSICAL MODEL FUNCTION.....	9-20
9.1	Data Matchup.....	9-20
9.2	L-band Geophysical Model Function.....	9-20
10	SCATTEROMETER WIND RETRIEVAL.....	10-24
11	ACKNOWLEDGMENT.....	11-26
12	REFERENCES AND CITATIONS.....	12-27

# 1 Scope

---

This document provides the theoretical basis of the algorithms used to produce the geolocated, calibrated  $\sigma_0$  and the ocean surface wind speed from the Level 1A Aquarius data.

The content covers the geometry, radiometric calibration, antenna polarization and Faraday rotation correction, radio frequency interference flagging and mitigation, geophysical model function, and retrieval algorithm of wind speed.

The algorithm flow and specification of software modules are described in the Scatterometer Science Processing Software (L1A\_to\_L2) User Manual, Project Document: AQ-485-0541 and JPL Document: D-51444.

## 2 Applicable Documents

Document	JPL Document Number	Aquarius Project Document Number
Aquarius Level 2A Science Requirements	D-29054	AQ-222-0039
Aquarius Science Calibration/Validation Plan	D-28229	AQ-212-0037
Aquarius Level 3 Science Algorithm Requirements	D-29053	AQ-322-0135
Aquarius Instrument Requirements Document	D-29007	AQ-325-0112

### 3 Introduction

---

Aquarius is a combined passive/active L-band microwave instrument developed to map the salinity field at the surface of the ocean from space [1]. The primary science objective of this mission is to monitor the seasonal and interannual variation of the large scale features of the surface salinity field in the open ocean with a spatial resolution of 150 km and a retrieval accuracy of 0.2 psu globally on a monthly basis. The measurement principle is based on the response of the L-band (1.413 GHz) sea surface brightness temperatures to sea surface salinity. To achieve the required accuracy, the impact of sea surface roughness, along with several additional factors impacting the observed brightness temperature, must be corrected to better than a few tenths of a degree Kelvin. To this end, Aquarius includes a scatterometer to help correct for this surface roughness effect.

The Aquarius instrument has three antenna beams, operating at about 29, 38 and 46 degrees [2]. Each antenna beam has one radiometer (1.413 GHz), which can acquire the first three Stokes parameters of microwave radiation. The antenna feeds are shared with the scatterometer (1.26 GHz), which acquires the normalized radar cross sections ( $\sigma_0$ ) for co- and cross-polarizations.

There are two baseline products from the Aquarius scatterometer: radar  $\sigma_0$  and ocean surface wind speed. The radar  $\sigma_0$  product will be radiometric calibrated and geolocated. The geophysical product derived from the scatterometer is the surface wind speed, representing the roughness of the sea surfaces and used for radiometer  $T_B$  corrections. This document provides the theoretical basis of the algorithms used to produce the geo-located, calibrated  $\sigma_0$  and the ocean surface wind speed from the Level 1A Aquarius data.

## 4 Geometry and Geo-location

---

The geometry computations begin with the interpolation of the spacecraft position, velocity, and attitude to the observation time. We use cubic splines to interpolate the ephemeris and attitude. The ephemeris is then converted from Earth Centered Inertial (ECI) coordinates to Earth Centered Earth Fixed (ECEF) coordinates.

### 4.1 Computation of Spacecraft Nadir Direction

We compute the location of spacecraft nadir point and ECEF position vector pointing from center of Earth to nadir point. The computed nadir point is the geodetic nadir, i.e. the location on the Earth ellipsoid such that the unit normal points directly to the spacecraft. The nadir longitude is computed directly from the spacecraft position  $x$  and  $y$  components. The geodetic nadir latitude and height above the ellipsoid is computed numerically with an iterative algorithm that is seeded with the geocentric nadir coordinates. After the computation of the geodetic latitude and longitude, the nadir position on Earth and then the ECEF nadir vector may be computed directly. The heritage of this algorithm is from SeaWinds and NSCAT [3].

### 4.2 Computation of Beam Bore-Sight Look Vector

In each of the 3 Aquarius beams, we construct a coordinate system where the  $z$ -axis points along bore-sight, the  $x$ -axis aligns with the H-polarization, and the  $y$ -axis aligns with V-polarization so that  $\hat{h} \times \hat{v}$  is the look direction. We call this coordinate system the antenna beam coordinates, and it is related to the antenna global coordinate system with the following transformation:

$$\begin{bmatrix} x_G \\ y_G \\ z_G \end{bmatrix} = M_{i,H}^B \begin{bmatrix} x_{i,B} \\ y_{i,B} \\ z_{i,B} \end{bmatrix}, \quad (4.1)$$

where

$$\begin{aligned} M_{1,H}^B &= \begin{bmatrix} -0.14228 & 0.98123 & -0.13017 \\ -0.98551 & -0.15270 & -0.07388 \\ -0.09237 & 0.11777 & 0.98874 \end{bmatrix} \\ M_{2,H}^B &= \begin{bmatrix} 0.22276 & 0.97487 & -0.00212 \\ -0.96420 & 0.22064 & 0.14709 \\ 0.14386 & -0.03072 & 0.98912 \end{bmatrix}. \\ M_{3,H}^B &= \begin{bmatrix} -0.09500 & 0.98767 & 0.12446 \\ -0.99358 & -0.08635 & -0.07313 \\ -0.06148 & -0.13061 & 0.98953 \end{bmatrix}. \end{aligned} \quad (4.2)$$

The antenna global coordinate system is related to the Instrument Coordinate System (ICS) by the following transformation:

$$\begin{bmatrix} x_I \\ y_I \\ z_I \end{bmatrix} = \begin{bmatrix} 0 & -1 & 0 \\ \cos(33) & 0 & \sin(33) \\ -\sin(33) & 0 & \cos(33) \end{bmatrix} \begin{bmatrix} x_G \\ y_G \\ z_G \end{bmatrix}. \quad (4.3)$$

The ICS has axes that are the same as the Observatory Coordinate System (OCS), however there is a shift in origin. The OCS has its y-axis coincident with the launch vehicle adapter's cylindrical line of symmetry and the long axis of the service platform with positive direction away from the launch vehicle adapter toward the service platform, the x-axis is parallel to the line containing the two solar array primary attach/hinge points, and the z-axis is perpendicular to both the x and z axes and positive towards the nominal nadir panel of the service platform. In Figure 4.1 we show a diagram of the OCS coordinate system [4].

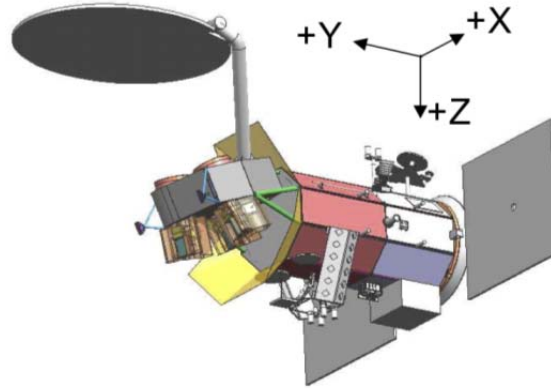


Figure 4.1: Diagram of the Observatory coordinate system. The instrument coordinate system has axes that are parallel to the OCS but has a different origin. +Z axis roughly points towards nadir and +X axis is roughly in the direction of spacecraft velocity (not exactly; depends on attitude angles).

The ICS is related to the orbital reference frame by the yaw, pitch and roll angles. Aquarius uses a geocentric orbital reference frame, defined by:

$$\begin{aligned} \hat{s} &= \hat{t} \times \hat{u} \\ \hat{t} &= \frac{\hat{u} \times \vec{V}_{sc}}{|\hat{u} \times \vec{V}_{sc}|} \\ \hat{u} &= -\frac{\vec{R}_{sc}}{|\vec{R}_{sc}|} \end{aligned} \quad (4.4)$$

where  $\vec{R}_{sc}$ ,  $\vec{V}_{sc}$  are the ECEF position and velocity vectors of the spacecraft. The transformation between the ICS and the orbital reference frame is given by:

$$\begin{bmatrix} x_{stu} \\ y_{stu} \\ z_{stu} \end{bmatrix} = (M_{rpy})^{-1} \begin{bmatrix} x_{ICS} \\ y_{ICS} \\ z_{ICS} \end{bmatrix}, \quad (4.5)$$

where the attitude rotation matrix  $M_{rpy}$  is given by

$$M_{rpy} = \begin{bmatrix} \cos y \cos p & \cos y \sin p \sin r + \sin y \cos r & -\cos y \sin p \cos r + \sin y \sin r \\ -\sin y \cos p & -\sin r \sin p \sin r + \cos y \cos r & \sin y \sin p \cos r + \cos y \sin r \\ \sin p & -\cos p \sin r & \cos p \cos r \end{bmatrix}, \quad (4.6)$$

where  $y$  is the yaw angle,  $p$  is the pitch angle, and  $r$  is the roll angle [5].

Once we have the look vector in the  $stu$  coordinates, we use the unit vectors of the local coordinates computed from the spacecraft position and velocity to obtain a vector in ECEF coordinates.

$$\begin{bmatrix} x_{ECEF} \\ y_{ECEF} \\ z_{ECEF} \end{bmatrix} = x_{stu} \hat{s} + y_{stu} \hat{t} + z_{stu} \hat{u} \quad (4.7)$$

The composition of all these rotations applied to  $l_B = [0 \ 0 \ 1]^T$  gives the look vector in ECEF coordinates.

### 4.3 Geolocation of Antenna Footprint on Earth

Given the ECEF spacecraft position  $(x_{sc}, y_{sc}, z_{sc})$  and ECEF beam bore-sight direction  $l = [l_x, l_y, l_z]^T$  [6], we may solve for the intersection of the beam with the Earth. We model the Earth as an ellipsoid where any point  $(x, y, z)$  on the surface of the ellipsoid satisfies the following equation:

$$\frac{x^2}{R_{eq}^2} + \frac{y^2}{R_{eq}^2} + \frac{z^2}{R_{polar}^2} = 1. \quad (4.8)$$

Here,  $R_{eq} = 6378137$  meters, and  $R_{polar} = 635675.2314245179$  meters. We seek the range,  $\rho$ , that satisfies the following equation:

$$\frac{(x_{sc} + \rho l_x)^2}{R_{eq}^2} + \frac{(y_{sc} + \rho l_y)^2}{R_{eq}^2} + \frac{(z_{sc} + \rho l_z)^2}{R_{polar}^2} = 1. \quad (4.9)$$

This reduces to a quadratic equation for  $\rho$ . If there are two real non-negative solutions, we pick the solution with the smallest  $\rho$ . If the solutions are imaginary or negative the beam is off-earth and the corresponding bit flag is set. The ECEF coordinates of the footprint are then

$$\begin{aligned} x_{fp} &= x_{sc} + \rho l_x \\ y_{fp} &= y_{sc} + \rho l_y \\ z_{fp} &= z_{sc} + \rho l_z \end{aligned} \quad (4.10)$$

The geocentric latitude,  $\phi_c$ , geodetic latitude,  $\phi$ , and longitude,  $\lambda$ , are computed as:

$$\lambda = \text{atan2}(y_{fp}, z_{fp})$$

$$\phi_c = \text{asin}\left(\frac{z_{fp}}{\sqrt{x_{fp}^2 + y_{fp}^2 + z_{fp}^2}}\right), \quad (4.11)$$

$$\phi = \text{atan}\left(\tan\left[\frac{\phi_c}{1 - \varepsilon^2}\right]\right)$$

where  $\varepsilon = \sqrt{1 - \left(\frac{R_{polar}^2}{R_{eq}^2}\right)}$  is the Earth eccentricity. The heritage of these algorithms is SeaWinds.

#### 4.4 Computation of Incidence Angle and Azimuth Angle

Given the ECEF vector of the beam footprint,  $r_{fp} = [x_{fp}, y_{fp}, z_{fp}]^T$ , we compute the unit normal to the ellipsoid by

$$\hat{n} = 2 \left[ \frac{x_{fp}}{R_{eq}}, \frac{y_{fp}}{R_{eq}}, \frac{z_{fp}}{R_{polar}} \right]^T. \quad (4.12)$$

We then compute the incidence angle as

$$\theta_{inc} = \text{acos}(\hat{n} \cdot \hat{l}_G).$$

The azimuth angle is the clockwise angle measured from North to the projection of the look vector onto the North-East plane at  $r_{fp}$ . We compute the transformation between ECEF coordinates and geographic coordinates (North-East-Down) as:

$$\begin{bmatrix} l_N \\ l_E \\ l_D \end{bmatrix} = \begin{bmatrix} -\sin \phi \cos \lambda & -\sin \phi \sin \lambda & \cos \phi \\ -\sin \lambda & \cos \lambda & 0 \\ -\cos \phi \cos \lambda & -\cos \phi \sin \lambda & -\sin \phi \end{bmatrix} \begin{bmatrix} l_x \\ l_y \\ l_z \end{bmatrix}, \quad (4.13)$$

where  $\phi$  is the geodetic latitude and  $\lambda$  is the longitude. Then the azimuth angle is computed as  $\text{atan2}(l_E, l_N)$ . The heritage of these algorithms is SeaWinds.

#### 4.5 Computation of Polarization Roll Angle

After geolocation, we compute the ground polarization directions as:

$$\hat{h}_{ground} = \frac{\hat{n} \times \hat{l}}{|\hat{n} \times \hat{l}|} \quad (4.14)$$

$$\hat{v}_{ground} = \hat{l} \times \hat{h}$$

Where  $\hat{n}$  is the unit normal to the ellipsoid and  $\hat{l}$  is the antenna beam look vector in ECEF coordinates. If we apply the same transformation matrices used to generate the look vector to the h-polarization unit vector in antenna beam coordinates,  $h_B = [1 \ 0 \ 0]^T$ , we generate the beam h-polarization unit vector in ECEF coordinates,  $h_{ECEF}$ . We then compute the polarization roll angle as:

$$\varphi_{pol} = -\text{atan2}\left(\hat{h}_{ECEF} \cdot \hat{h}_{ground}, \hat{h}_{ECEF} \cdot \hat{v}_{ground}\right). \quad (4.15)$$

## 4.6 Computation of Beam Edge Points

We read in the antenna pattern files for the scatterometer frequency, and compute the off-nadir angles such that the co-polarization two-way gain is three dB down from the peak gain. We do this every 90 degrees in the azimuthal coordinates of the beam. We then compute a look vector for each of these directions and geolocate them to generate the beam edge points contained in the Aquarius L2 data product.

## 5 Radiometric Calibration

---

### 5.1 Calibration Equation

The radiometric calibrated normalized radar cross-section ( $\sigma_0$ ) is expressed in terms of parameters either measured by Aquarius or derivable from geometry (Section 4) and pre-launch test measurements:

$$\sigma_{0ij} = \frac{P_{sij}}{P_{cal} X_{gij} X_{cij}} \quad (5.1)$$

where the subscripts,  $i$  and  $j$ , indicate the beam number and polarization. On the right hand side of the equation,  $P_s$  is the estimated echo power, related to the signal plus noise measurements and noise only measurements performed by Aquarius scatterometer:

$$P_s = P_e - P_n \quad (5.2)$$

The power measurements performed by Aquarius on-orbit are

$P_{cal}$	The measured power of a loop-back pulse.
$P_e$	The measured power of radar signal and system noise
$P_n$	The measured power of noise-only measurements

$P_{cal}$  is proportional to the radar transmit power and receiver gain, and is measured for each radar transmit pulse. It will allow the removal of transmit power and receiver gain drift over time for on orbit radiometric calibration.

There are two other radiometric calibration factors:  $X_{gij}$  concerns the geometry and antenna pattern effects and  $X_{cij}$  involves the radiometric gain and loss parameters.

$$X_{gij} = \frac{A_{3dB} K_{ij}}{R_c^4} \quad (5.3)$$

In the above equation,  $A_{3dB}$  is the footprint area bounded by the 3-dB beamwidth,  $K_{ij}$  accounts for the antenna pattern integration effects, and  $R_c$  is the slant range from the spacecraft to the center of antenna footprint. We find that  $K_{ij}$  can be parameterized with high accuracy as a function of incidence angle and spacecraft latitude for each antenna beam and polarization. The lookup table for  $K_{ij}$  is pre-calculated using the antenna pattern from the scale model measurements.

The other calibration factor is related to various loss factors in the scatterometer electronics and peak gain of antenna.

$$X_{cij} = \frac{\lambda^2}{(4\pi)^3} \frac{L_{lbc} L_{cal} G_{bp}^2}{L_{op} L_T L_R B_{ij}} \quad (5.4)$$

These loss factors are defined in the following table

$L_{lbc}$	Loss through the Loop-back attenuator
$L_{cal}$	Loss through the variable attenuator during a loop-back calibration pulse.
$L_{op}$	Loss through the variable attenuator during measurement pulses.

$L_T$	Loss of the transmit path from the loop-back coupler in the SFE to the antenna
$L_R$	Loss of the receive path from the antenna to the loop-back in the SFE
$G_{bp}$	Antenna peak gain
$B_{ij}$	Bias terms to compensate for accumulated (but constant) measurement error

Note that all the pre-launch measurements are limited by the accuracy of test equipment. There are bias errors associated with each loss and gain measurement. To account for the measurement errors, we introduce a bias adjustment correction factor ( $B_{ij}$ ). We cannot determine or improve the accuracy of  $B_{ij}$  post-launch using the Aquarius data alone. We will cross-calibrate the Aquarius data with the Japanese PALSAR data to determine the  $B_{ij}$  factor.

## 5.2 Look-up Table for K-factor

It is very time consuming to carry out the 2-d numerical integration ( $X_{gij}$ ) for all orbit steps and attitude. It is necessary to develop a look-up table, which will be practical for in-line data processing. We use the scatterometer simulator to carry out the  $X_{gij}$  integration for many orbits and a range of spacecraft attitude.

$$X_{gij} = \frac{1}{T} \int \int \int_{area} \frac{g_r g_t h(t - \frac{2R}{c}) dA}{R^4} dt \quad (5.5)$$

In the integral,  $g_r$  and  $g_t$  are the antenna pattern for receive and transmit. The function “h” accounts for the radar transmit pulse shape, receiver range gate and time delay. “T” is the width of range gate. Therefore we obtain the values of  $X_{ij}$  and  $K_{ij}$  in the seven dimensional space: beam# (i), polarization (j), latitude, longitude, yaw, roll, and pitch.

$$K_{ij}(lat, lon, yaw, roll, pitch) = \frac{R_c^4(lat, lon, yaw, roll, pitch)}{A_{3dB}(lat, lon, yaw, roll, pitch)} X_{gij}(lat, lon, yaw, roll, pitch) \quad (5.6)$$

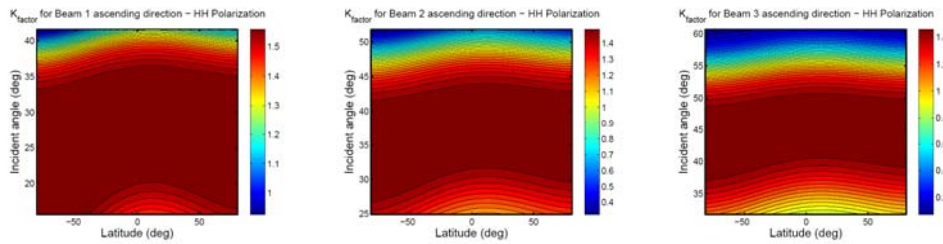


Figure 5.1 Illustration of the K-factor table for three antenna beams for HH polarization.

We find that the effects of longitude, yaw, roll and pitch can be accurately accounted for by one parameter, incidence angle, which is also computed using the scatterometer orbit simulator and processor. In summary, the K-factor can be parameterized effectively with 4 parameters: beam#, polarization, latitude, and incidence angle.

$$K_{ij} = K_{ij}(lat, \theta) \quad (5.7)$$

To account for minor variations along the satellite track, we introduce the latitude as a modeling parameter and use two look-up tables – one for ascending and one for descending.

In comparison with the full scalar radar equation integration, the error in the K-factor approximation is  $< 0.01$  dB. Fig. 5.1 illustrates the K-factor table for the HH polarization for all three antenna beams.

## 6 Antenna Polarization and Faraday Rotation Correction

### 6.1 Antenna Polarization Correction

We employ an explicit least-squares-fit to determine the antenna polarization correction. We simulated 120 orbits of data nominally and with the cross-pol terms in the Mueller matrix for antenna gain explicitly set to zero. This is done in such a way to preserve total sigma0 at level 2. We then process both sets of simulated data to Level 2 using L1A\_to\_L2 software.

We perform a least-squares fit of the following model to two sets of processed level 2  $\sigma_0$  data:

$$\sigma_0^{HV,no-xtalk} = \sigma_0^{HV,xtalk} + \alpha\sigma_0^{HH,xtalk} + \beta\sigma_0^{YV,xtalk} \quad (6.1)$$

where  $\sigma_0^{HV,xtalk}$  is the symmetrized cross-pol observation in the presence of antenna polarization cross-talk,  $\sigma_0^{HV,no-xtalk}$  is the symmetrized cross-pol observation in the absence of cross-talk, and  $\alpha, \beta$  are the fitting parameters. After we compute  $\alpha, \beta$ , we perform another least-squares fit

$$\sigma_0^{HH,no-xtalk} = \sigma_0^{HH,xtalk} + A(1 - \gamma) \quad (6.2)$$

$$\sigma_0^{YV,no-xtalk} = \sigma_0^{YV,xtalk} + A\gamma$$

where  $\gamma = 2(\sigma_0^{HV,xtalk} - \sigma_0^{HV,no-xtalk})$  is the excess  $\sigma_0$  that we must distribute into the co-polarized channels. Note that  $\alpha$  and  $\beta$  are typically negative corresponding to a reduction in the cross-polarized power. Below is a table of the ( $\alpha, \beta, \gamma$ ) values as implemented in “L1A\_to\_L2/L2\_APC\_matrix\_scale\_model\_3-18-2010.”

As of 3-30-2010	$\alpha$	$\beta$	$\gamma$
Beam 1	-0.005585	-0.001394	0.4569
Beam 2	-0.000579	-0.004066	0.2804
Beam 3	-0.000178	-0.004613	0.4302

The least squares fits described above can be written in the following form:

$$\begin{pmatrix} \sigma_0^{HH,TOI} \\ \sigma_0^{HV,TOI} \\ \sigma_0^{YV,TOI} \end{pmatrix} = APC \begin{pmatrix} \sigma_0^{HH,ANT} \\ \sigma_0^{HV,ANT} \\ \sigma_0^{YH,ANT} \\ \sigma_0^{YV,ANT} \end{pmatrix}, \quad (6.3)$$

where APC is a matrix with 3 rows and 4 columns, and TOI is short for top-of-ionosphere. Note that sigma0 TOI is not a L2 product, it is only used as an intermediate in the calculations. In terms of ( $\alpha, \beta, \gamma$ ) we may write the APC matrix as

$$APC = \begin{bmatrix} 1 - 2\alpha(1 - \gamma) & 0.0 & 0.0 & -2\beta(1 - \gamma) \\ \alpha & 0.5 & 0.5 & \beta \\ -2\alpha\gamma & 0.0 & 0.0 & -2\beta\gamma \end{bmatrix}. \quad (6.4)$$

The L1A\_to\_L2 software reads an ASCII file at run-time, which contains the APC matrix in the above format (i.e. matrix elements, not  $\alpha, \beta, \gamma$ ). The ASCII file is specified by the command line option ‘-apc\_file apc\_filename’.

## 6.2 Faraday Rotation Angle Estimation

We estimate the one-way Faraday rotation angle,  $\theta_F$ , using the IONEX [7] vertically integrated TEC data and the IGRF-11 model for the Earth's magnetic field [8]. If we assume a constant electron-density profile and constant Earth magnetic field along the slant path from spacecraft to ground, then we have [9]

$$\theta_F = 2.6 \times 10^{-13} \text{TEC}_{\text{slant}} B \lambda^2 \cos \chi, \quad (6.5)$$

where  $\text{TEC}_{\text{slant}}$  is the total electrons per square meter along the slant path,  $B$  is the Earth's magnetic field in Tesla,  $\lambda$  is the radar wavelength in meters, and  $\chi$  is the angle between the radar look direction and the magnetic field. We approximate  $\text{TEC}_{\text{slant}} = 0.75 \text{VTEC} / \cos \varphi$  where VTEC is the vertically integrated TEC (up to GPS altitudes),  $\varphi$  is the off-nadir look angle of the antenna, and  $\theta_F$  is the Faraday rotation angle in degrees.

## 6.3 Faraday Rotation Correction

Faraday rotation is significant at L-Band frequencies [10,11] and significantly increases the cross-polarization signal for Aquarius. An exact correction for Faraday rotation may only be performed if the full polarimetric covariance matrix is observed. However, Aquarius only observes the diagonal part of the polarimetric covariance matrix so we must employ a model to remove cross-polarization coupling due to Faraday rotation. We use the following model [12]:

$$\begin{aligned} \sigma_0^{HH,M} &= \sigma_0^{HH,TOA} \cos^4 \theta_F + \sigma_0^{VV,TOA} \sin^4 \theta_F - 2\rho_{HHVV} \cos^2 \theta_F \sin^2 \theta_F \sqrt{\sigma_0^{HH,TOA} \sigma_0^{VV,TOA}}, \\ \sigma_0^{VV,M} &= \sigma_0^{HH,TOA} \sin^4 \theta_F + \sigma_0^{VV,TOA} \cos^4 \theta_F - 2\rho_{HHVV} \cos^2 \theta_F \sin^2 \theta_F \sqrt{\sigma_0^{HH,TOA} \sigma_0^{VV,TOA}}, \end{aligned} \quad (6.6)$$

where  $\rho_{HHVV}$  is the HH-VV correlation,  $\sigma_0^{HH,M}$ ,  $\sigma_0^{VV,M}$ , are the model measurements in the presence of Faraday rotation, and  $\sigma_0^{HH,TOA}$ ,  $\sigma_0^{VV,TOA}$ , are the Faraday rotation corrected measurements. We use a numerical method to find the values of  $\sigma_0^{HH,TOA}$ ,  $\sigma_0^{VV,TOA}$  that minimize the following cost function:

$$J(\sigma_0^{HH,TOA}, \sigma_0^{VV,TOA}) = \left[ \sigma_0^{HH,TOI} \ln \left( \frac{\sigma_0^{HH,TOI}}{\sigma_0^{HH,M}} \right) \right]^2 + \left[ \sigma_0^{VV,TOI} \ln \left( \frac{\sigma_0^{VV,TOI}}{\sigma_0^{VV,M}} \right) \right]^2. \quad (6.7)$$

We use the limited memory BFGS method to minimize the cost function [13]. The algorithm requires the cost function and its gradient to be supplied. The gradient is straightforward to compute from  $J$  and will not be done here. Minimization of the cost function gives us the Faraday corrected values for  $\sigma_0^{HH,TOA}$ ,  $\sigma_0^{VV,TOA}$ . After we obtain these Faraday-rotation corrected NRCS for HH and VV, we obtain the symmetrized HV channel via conservation of total sigma0, we find

$$\sigma_0^{HV,TOA} = 0.5(\sigma_0^{HH,TOI} + \sigma_0^{VV,TOI} + 2\sigma_0^{HV,TOI} - \sigma_0^{HH,TOA} - \sigma_0^{VV,TOA}). \quad (6.8)$$

## 7 Land and Sea Ice Fractions

---

The scatterometer land and ice fractions are generated by a gain-area-range weighted integration over the Aquarius antenna beam footprint on the ground and a high-resolution land or sea ice data product. For land we use a land flag originally developed for MODIS data processing [14] which is posted at every 1/128 degree in latitude and longitude. For sea ice we use the operational NCEP data product provided at <http://oceandata.sci.gsfc.nasa.gov/Ancillary/Meteorological/> which is posted at every 1/12 degree in latitude and longitude. For every Aquarius footprint we compute:

$$F = \frac{\int_A dA \left( \frac{h}{\rho^4} \right) |g|^2 \eta}{\int_A dA \left( \frac{h}{\rho^4} \right) |g|^2} \quad (7.1)$$

where A is the area on Earth contained within 10 deg off bore-sight, g is the antenna gain, h represents range-gating effects,  $\rho$  is the range, and  $\eta$  is the land / sea-ice mask value.

We discretize this integral and use a relatively coarse integration step size to facilitate quick computation of this land / sea-ice fraction. In the beam coordinate system, we discretize the angular coordinates as show in Figure 7.1. The cell with center at coordinate  $(\theta_c, \varphi_c)$  is composed of a trapezoid with vertices located at coordinates  $(\theta_i, \varphi_i)$  for  $i=1, \dots, 4$

$$\begin{aligned} \theta_1 &= \theta_c - \delta_\theta / 2; \varphi_1 = \varphi_c + \delta_\varphi / 2; \\ \theta_2 &= \theta_c - \delta_\theta / 2; \varphi_2 = \varphi_c - \delta_\varphi / 2; \\ \theta_3 &= \theta_c + \delta_\theta / 2; \varphi_3 = \varphi_c - \delta_\varphi / 2; \\ \theta_4 &= \theta_c + \delta_\theta / 2; \varphi_4 = \varphi_c + \delta_\varphi / 2; \end{aligned} \quad (7.2)$$

Next we project the center of each cell and the 4 corners from the beam coordinate system onto the Earth. The area of the cell on the Earth may be computed from the corners using spherical trigonometry. We use the cell center geolocation to compute the range and land / sea-ice flag value. For the land and sea-ice fraction computation we use step sizes of 1 degree in  $\theta$  and 5 degrees in  $\varphi$ .

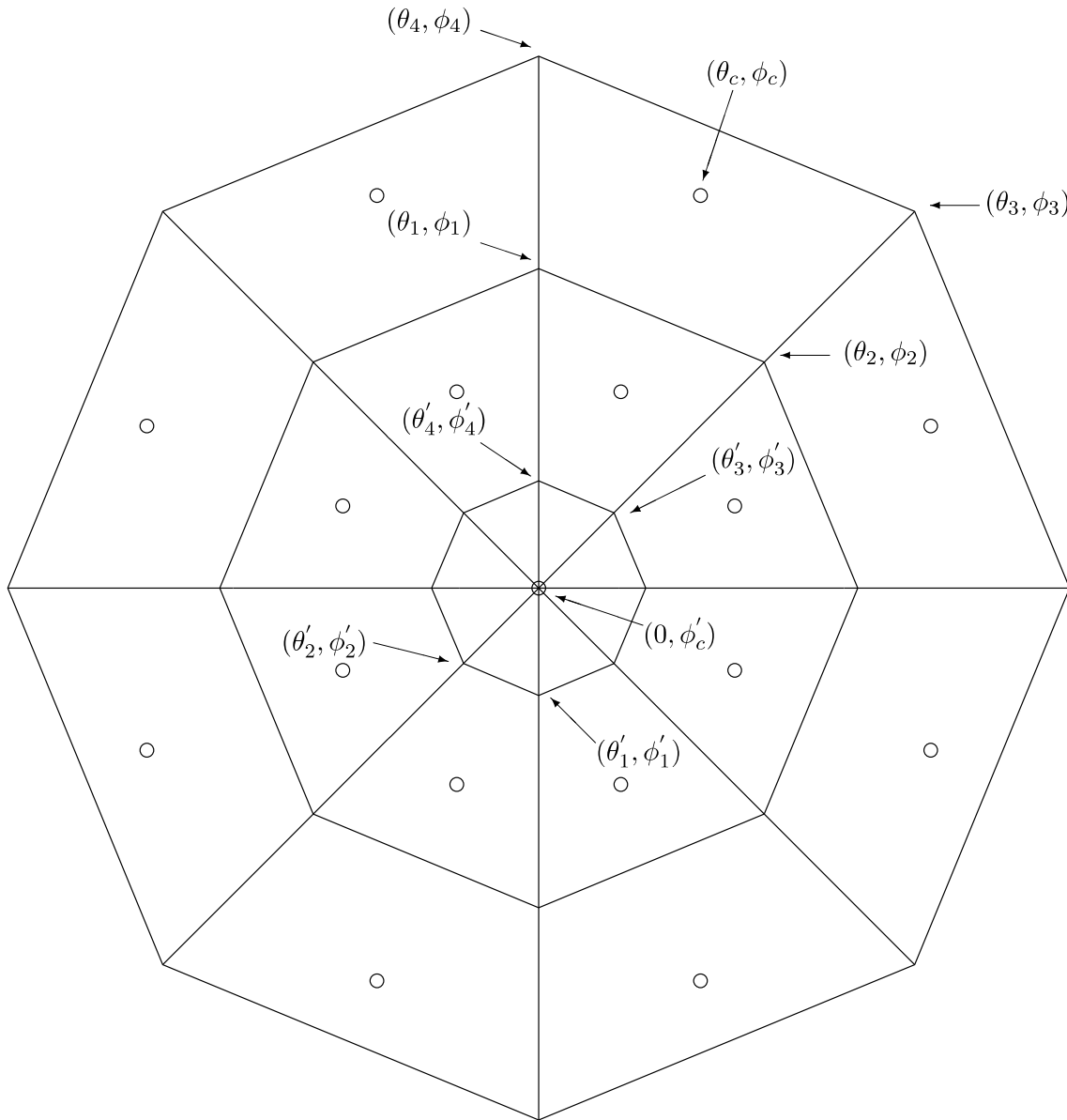


Figure 7.1 Diagram of beam cells, with cell centers and corners of each cell plotted. We illustrate two cases: the case where the cell center is not in the center of the beam and the case where it is.

## 8 RFI Flag and Mitigation

---

The Aquarius scatterometer processing algorithm depends on two techniques to detect and mitigate the effects of radio-frequency interference (RFI) within the scatterometer echo and noise channels. One method is based on a sensitive, on-board, RFI flagging technique, and the other is a ground-based, outlier flagging technique.

### 8.1 Onboard RFI Detection

The onboard detection scheme was implemented based on the need to detect low levels of RFI that could affect the accuracy of weak ocean echoes. The technique depends on the fact that low-level RFI can be sensed easily at the high-time resolution of the digital detection hardware, but can be very difficult to detect after a signal has been averaged over the onboard integration window. The technique is effectively a coarse PDF computation, looking for small numbers of outliers to a normal Gaussian distribution due to instrument and ambient thermal noise.

The sensitivity parameters for this on-board algorithm are adjustable by ground command. The challenge lies in picking a set of parameters that will be as sensitive as possible to the most common RFI (usually short duration, moderate-to-high amplitude sinusoidal signals) without being triggered by the Gaussian noise distribution and generating false-positive RFI flags. The other major limitation of this technique is that it can only be used in the noise-only detection windows, where the ambient thermal noise power is predictable. In echo windows, the returned power varies from the thermal noise level to very high levels due to rough ocean and land backscatter. Here, the on-board RFI flagging approach cannot be used. But, by design, the echoes are interspersed with noise-only windows of the same polarization with gaps of  $\sim 10$  ms, under the assumption that RFI may often appear in echo and adjacent noise-only windows for many RFI sources.

The analog-to-digital converter (ADC) samples the receive power at 16 MHz over a 2-3 ms receive window. The user specifies a power level and a number of digital counts that exceed this level. If the digital hardware detects the specified number of counts exceeding the specified power level, and RFI flag is set on board and transmitted to the ground (see Figure 1). All measurements at this time and polarization (two echo and one noise measurements within a 30 ms period) are excluded from ground analysis if the noise-only measurement is flagged for RFI. Another limitation of this technique is that the thresholds are optimized for detection of RFI of a certain character. The default onboard power threshold of  $\sim 14$  mV rms into the ADC corresponds to a received power level at the antenna of -120 dBW, approximately three-sigma above the receiver noise floor level. About 100 ADC samples (0.3%) should exceed this power level for a typical receive window. The most numerous RFI sources have pulse lengths of about 100  $\mu$ s, generating about 800 ADC samples that exceed the threshold. The default trigger count is therefore set to 400 ADC samples, ensuring a negligible number of false alarms.

RFI of an equivalent integrated power can escape detection if it is of lower power level and longer duration, or if it is of higher power and shorter duration. Both types of RFI sources exist, but are thought to be less common. It is possible to change the threshold and trigger count parameters to be sensitive to these types of RFI, but this has not been exercised since the ground-based RFI detection scheme was determined to be necessary for the following reasons.

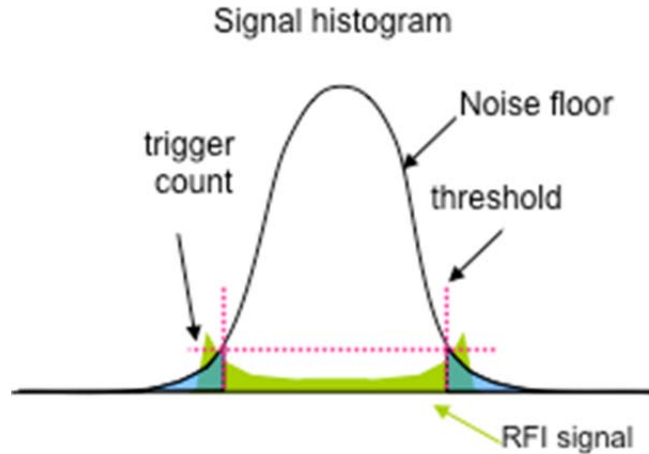


Figure 8.1. RFI detection model: Sensing a low-level CW RFI signal with a Gaussian thermal-noise envelope. Two parameters are needed: A threshold level and a trigger count.

Once Aquarius was in orbit, it was quickly observed that much obvious (and presumably subtle) RFI was escaping detection by the on-board RFI flagging technique. Many strong RFI sources were appearing in echo windows but not in adjacent noise-only windows. This is most likely due to “frequency hopping” by the ground transmitters, where adjacent RFI pulses hop around in frequency and pulses a few milliseconds apart can differ substantially in frequency, with one pulse lying in the Aquarius 5 MHz receive band and the adjacent pulses lying outside of this band, thus escaping detection by Aquarius. Also, some of the Aquarius on-board RFI flags cannot be used because the radiometer correlated noise diode (CND) fires within the noise window, setting off the RFI flag. This occurs in alternating V-pol noise only windows, by design. Thus, true RFI cannot be detected in these 30-ms echo-noise-echo sequences. Finally, it is apparent that in certain parts of the world, RFI sources are not setting off the on-board flags at all, implying that the RFI sources have power levels or pulse widths that the default detection scheme cannot detect.

On the other hand, the on-board RFI detection scheme does detect a significant amount of low-level RFI that is not obvious and cannot be detected by a ground-based detection scheme. This is almost certainly real RFI and not false positive detections, as they occur primarily over RFI-dense land and near-land areas, and rarely if ever over open ocean.

## 8.2 Ground-Based RFI Detection

The ground-based RFI detection technique is an outlier detection algorithm. It is performed in several steps as discussed below, and has a number of adjustable parameters. These parameters have been chosen somewhat ad-hoc and appear to work reasonably well, but future work may suggest parameter adjustments to improve performance.

In step 1, all valid on-orbit RFI flags are used. Any noise-only measurement that appears to be RFI (except alternating V-pol noise-only measurements in which the CND fires) is flagged as RFI, as are adjacent co-pol and cross-pol echo measurements.

In step 2, all noise-only measurements that exceed a certain power level are flagged as RFI (note that these are the several millisecond-long integrated measurements, not the high-time resolution on-board ADC samples). The levels in use currently are -33 dBm for the non-CND noise-only

channels, and -31 dBm for the V-pol CND noise-only channels. Note that most of these points have already been flagged as RFI by the on-board algorithm, but a significant number have escaped that detection because the RFI pulse characteristics are not captured by the default threshold parameters described above.

In step 3 we perform a running “exclusive-median” filtering of the data. We pass through the data estimating the median value of a window of points around each test point, excluding the test point. We also estimate the standard deviation about the mean of these points, again excluding the test point. In our current implementation, we use 7 points on each side of the point under test to estimate the median, mean, and standard deviation. This estimation is done for every measurement type: each co-pol, cross-pol, and noise-only data series for each polarization on each of the three antenna beams. V-pol noise-only series are split into V-noise with CND and V-noise without CND series for this analysis. These computations are done in linear, rather than dB, power units.

In step 4, we perform an initial outlier RFI-flagging test. If the absolute value of the difference between the point under test and the adjacent-points median value exceeds a certain number of standard deviations, the test point is flagged as RFI (i.e., if  $|\text{test} - \text{median}| > N * \text{stdev}$ , flag as RFI). We limit the maximum standard deviation value to use in the test, as some land regions are so dense with RFI that the standard deviations end up being huge and corrupted by RFI; in these cases, by limiting the standard deviation value to use, all the data are correctly flagged as RFI. In the current implementation, the maximum standard deviation is 0.001 mW, while the number of standard deviations is chosen to be 6 for all co-pol and cross-pol channels, and 5 for both of the V-pol noise-only series and the H-pol noise-only series.

In step 5, we replace all RFI flagged points with their corresponding median-filtered values and then repeat step 3. We compute new exclusive median values and standard deviations about all test points. Since we have already flagged the most obvious RFI in step 4, this step is used to detect more subtle RFI.

In step 6, we repeat step 4, again flagging any outliers exceeding the thresholds or maximum standard deviation level as RFI. We currently use the same threshold levels here as in step 4. At this point, we have flagged the vast majority of outliers as RFI. Only in regions of relatively dense RFI do some probable RFI outliers make it through the filtering. However, low level RFI that does not manifest as obvious outliers cannot be detected by this process.

In step 7, we adjust the values of any noise-only measurements flagged as RFI. We replace the flagged values with median-filtered values. Since one of the following steps in normal scatterometer data processing is to subtract the noise-only measurement from the adjacent co- and cross-pol echo measurements, RFI-tainted noise-only measurements can result in incorrect negative sigma-0 estimates. Alternatively, we could automatically flag any echo adjacent to any flagged noise-only measurement as RFI and exclude it from further processing, but this ends up excluding a lot of potentially valid data, especially in areas of moderate-density RFI.

In subsequent processing, any measurement flagged with RFI is not used in computing 1.44 second averaged data, and the number of measurements used to compute the average is indicated in an additional averaging flag. If all measurements in a 1.44 second average are flagged with RFI, then they are all used in the average, and this is so noted in the averaging flag.

### **8.3 RFI Flagging Results**

The results of the RFI flagging algorithm are captured in a flag in the intermediate, internal L1B product. This flag documents whether the measurement contains no detectable RFI (flag value 0), whether the measurement has been flagged with RFI by the onboard algorithm only (flag

value 1), whether the measurement has been flagged with RFI by the ground-based algorithm only (flag value 2), or whether the measurement has been flagged with RFI by both on-board and ground-based algorithms (flag value 3).

RFI flagged by the on-board flagging only are typically RFI sources too weak to be detected by the ground-based outlier detection method. Yet these are strong enough to potentially affect the required accuracy level of the averaged data product. RFI flagged by the ground algorithm only typically appears in the echo channels rather than the noise-only channel, or is generated by RFI sources missed by the on-board algorithm. RFI flagged by both algorithms tends to appear in the noise-only channels and is relatively strong. Figure 2 shows a map of the distribution of RFI flags for a typical 7-day global measurement cycle. For the HH polarization channel, over half of the RFI detected on the ground is flagged by the on-board algorithm. For the VV channel, less than half is flagged on board due the exclusion of CND-induced onboard RFI flags. Beam 3, with the longest receive window, typically contains the most RFI while beam 1, with the shortest receive window contains the least RFI.

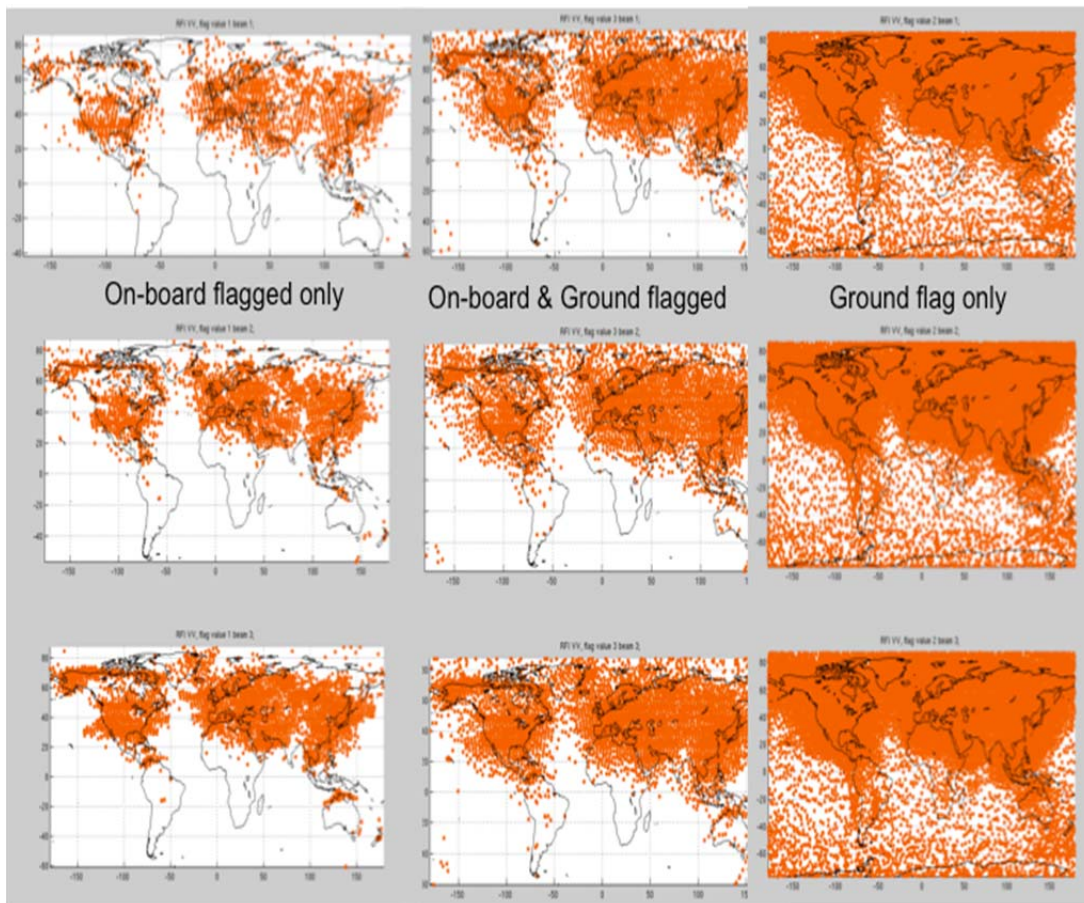


Figure 8.2. Geographic distribution of RFI locations in the VV channel as flagged by the on-board algorithm and ground-based algorithm.

## 9 Geophysical Model Function

---

We develop an empirical geophysical model function (GMF), relating the Aquarius radar  $\sigma_0$  to ocean surface winds, for the retrieval of surface wind from the scatterometer  $\sigma_0$ . The approach for constructing the empirical function is the same as that used for the SeaWinds and NSCAT scatterometer missions. There are two steps for this approach with step 1 for the development of a matchup dataset and step 2 for the derivation and model coefficients.

### 9.1 Data Matchup

The matchup dataset include the Aquarius data, the SSM/I F17 wind speed and rain rate and the wind vectors from NCEP. The SSM/I F17 and Aquarius data acquired within one hour from each other are collocated. The SSM/I F17 retrievals are reported on 0.25 degree latitude and longitude grids. Because the Aquarius footprint size is about 100 km, we average all the SSM/I data grids within 25 km from the center of Aquarius footprint.

The matchup of NCEP winds and Aquarius data has been routinely performed by the Aquarius Data Processing System (ADPS). The NCEP winds are reported every six hours on 1-deg grid resolutions, and are linearly interpolated in time and bilinearly interpolated in space to match up with the Aquarius observations. In addition to the NCEP winds, ADPS has been matching up the Reynolds Sea Surface Temperature (SST) and Hybrid Coordinate Ocean Model (HYCOM) SSS, which along with the NCEP wind matchups are available in the Aquarius L2 files.

To minimize the effects of rain, we excluded any matchups with non-zero SSM/I rain rate from the data analysis. The rain-free matchups were grouped into bins at  $1 \text{ m s}^{-1}$  in speed and 10 degrees in wind direction steps. The Aquarius data in each bin were averaged to represent the expected microwave response at the given wind speed and direction.

Figure 9.1 illustrates the VV and HH radar backscatter versus the relative wind direction for 5-, 8-, 10-, 12-, 15- and 20- $\text{m s}^{-1}$  SSM/I wind speeds. Each wind speed panel has three rows for the three antenna beams. There is clear wind direction dependence in the radar  $\sigma_{0s}$  for both polarizations at all wind speeds. The peak-to-peak variations are about 4 dB peak-to-peak at 20  $\text{m s}^{-1}$ , which agree very well with the aircraft observations [15]. However, the directional signals at 5  $\text{m s}^{-1}$  wind speed with a peak-to-peak amplitude of 0.7 dB have a negative upwind-crosswind (UC) asymmetry with the  $\sigma_{0s}$  at crosswind ( $90^\circ$  and  $270^\circ$ ) larger than that at upwind ( $0^\circ$ ) or downwind ( $180^\circ$ ), while the UC asymmetry is positive at above 10  $\text{m.s}^{-1}$  wind speeds. This feature was seen in the PALSAR HH data [16], but now also confirmed for the VV polarization. A close inspection of the data from 5 to 10  $\text{m s}^{-1}$  indicates that the upwind and downwind  $\sigma_{0s}$  grow with wind speed, while the crosswind  $\sigma_{0s}$  appears to decrease. The beam-2 and -3 VV data at 8  $\text{m s}^{-1}$  wind speed in fact feature four peaks with two small peaks at upwind and downwind in addition to the two small peaks at the crosswind directions.

### 9.2 L-band Geophysical Model Function

The matchup data using either SSM/I or NCEP wind for binning have been used to develop the GMFs for Aquarius, which relate the microwave backscatter to the wind speed ( $w$ ) and direction ( $\phi$ ), which is the wind direction relative to the radar look angle. We use the following cosine series for the modeling of radar data:

$$\sigma_{VV}(w, \phi) = A_{0VV}(w)[1 + A_{1VV}(w) \cos \phi + A_{2VV}(w) \cos 2\phi] \quad (9.1)$$

$$\sigma_{HH}(w, \phi) = A_{0HH}(w)[1 + A_{1HH}(w) \cos \phi + A_{2HH}(w) \cos 2\phi] \quad (9.2)$$

Here  $\sigma_{VV}$  and  $\sigma_{HH}$  are the normalized radar backscatter cross-section for V-transmit/V-receive and H-transmit/H-receive, respectively, and the A coefficients are estimated independently for each of Aquarius' antenna beam (incidence angle).

The modeling ( $A_0$ ) coefficients for VV and HH are illustrated as a function of the SSM/I or NCEP wind speed in the upper row of Fig. 9.2. The HH  $A_0$  agrees very well with PALSAR's GMF for all antenna beams for up to 15 m.s<sup>-1</sup> wind speeds. Beyond that Aquarius' GMF should be more accurate because the PALSAR GMF was constructed with much less matchups with the ASCAT winds above 20 m/s. The results from the SSM/I and NCEP matchups are very similar. Note that the natural values of  $A_0$  are illustrated, not the dB values. In general  $A_0$  increases with wind speed, but seems to have a relatively smaller rise in the range of 4 to 8 m.s<sup>-1</sup>. In particular,  $A_0$  for beam 3 VV has almost no response to wind speed within this range of wind speed, but seems to pick up an increasing trend above 10 m.s<sup>-1</sup>.

The  $A_1$  coefficients in the middle row of Fig. 9.2 increase with wind speed. The black and red solid curves in the panels are the piecewise-linear interpolation of the data points. The agreement with the PALSAR  $A_1$  is very good although the Aquarius data do indicate deviations from the linear increase. It is noted that  $A_1$  for VV is smaller by about a factor two than that for HH. Comparing the  $A_1$  between antenna beams (middle-left to middle-right panels) suggests an increase in  $A_1$  versus incidence angles. The characteristics of polarization and incidence angle dependence are consistent with those at C- and Ku-band frequencies.

The characteristics of  $A_2$  are illustrated in the bottom row of Fig. 9.2. There is not much difference between VV and HH, suggesting that the upwind-crosswind differences are essentially driven by the same scattering mechanisms for both polarizations. As we have discussed earlier, the  $A_2$  coefficients have a phase transition from negative to positive at about 8 m.s<sup>-1</sup> wind speed. Overall Aquarius'  $A_2$  for HH agrees reasonably well with PALSAR's, particularly for beam 2, while the difference with PALSAR is larger for beam 3 although the shapes of the curves for  $A_2$  versus wind speed are similar. The difference at wind speed lower than 5 m.s<sup>-1</sup> is likely caused by the use of different wind product for matchup: PALSAR analysis used the ASCAT wind for matchup [4], neither SSMI nor NCEP. The Aquarius data acquired at very low wind speeds suggest that there is a positive to negative transition at about 3 m.s<sup>-1</sup>. The NUC scattering mechanism causing the negative  $A_2$  over 3 to 8 m.s<sup>-1</sup> is unknown at this point.

The decrease of the directional harmonics ( $A_1$  and  $A_2$ ) for very high winds was suggested by higher frequency microwave measurements and PALSAR's  $A_2$  coefficients (blue curves in the bottom panel of Fig. 9.2), which all suggested that the ocean surfaces and waves will become less and less directional above a certain threshold wind speed, which is about 20 m.s<sup>-1</sup>.

The above model functions are evaluated for each Aquarius antenna beam or incidence angle. The current form of GMFs includes a set of text tables with the model coefficients ( $A_n$ ) tabulated at 1 m s<sup>-1</sup> step together with cubic spline interpolation between wind speed steps. We have examined the polynomial fitting of the modeling coefficients versus wind speed, and found that the fifth order polynomial fit can provide a very good representation from 0 to 25 m/s wind speed. However, when applied to the retrievals, the polynomial fit does not provide as accurate results as the tabular format with linear interpolation.

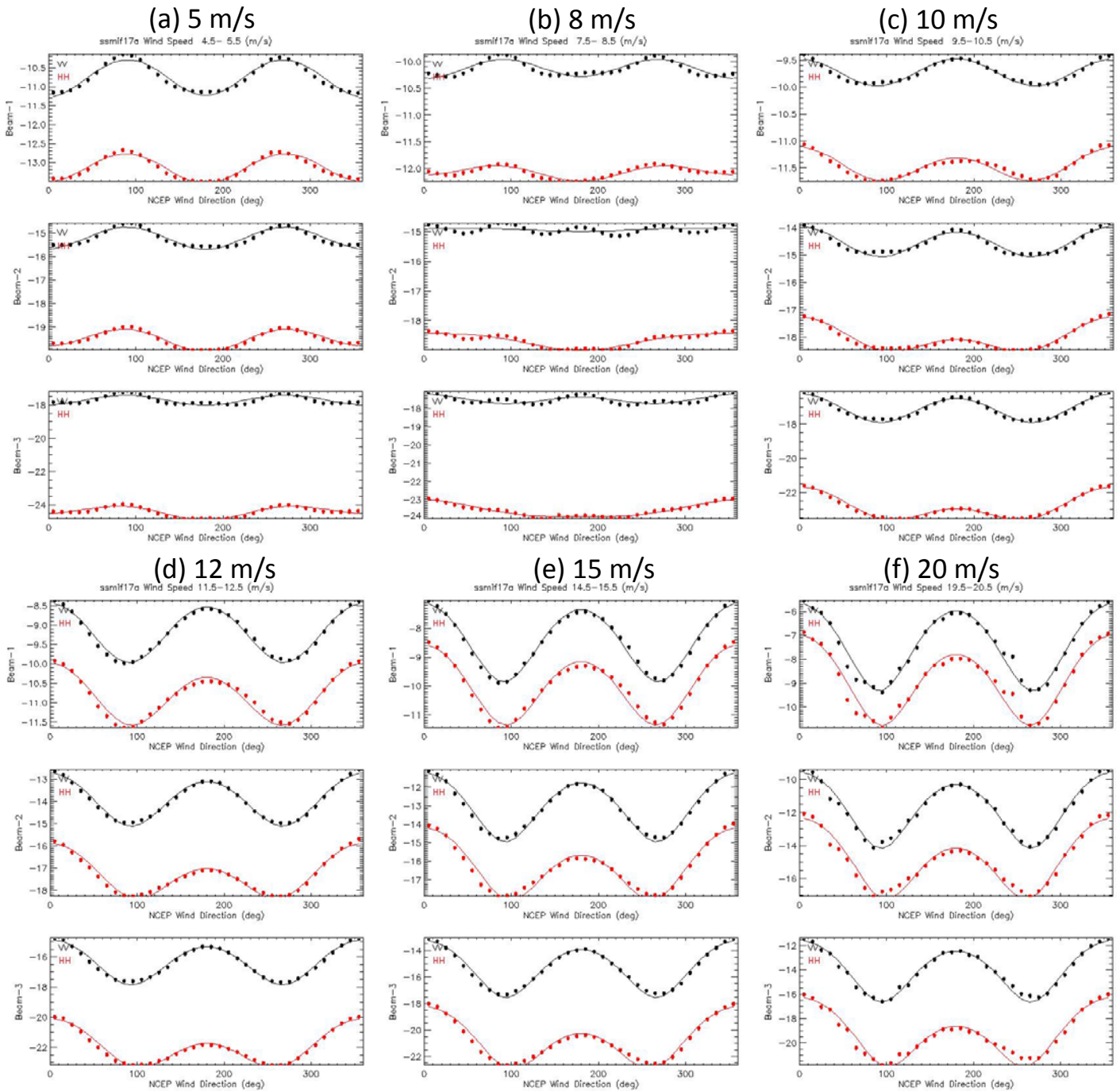


Figure 9.1. The Aquarius radar backscatter vs. NCEP wind direction for six SSM/I wind speeds. In each wind speed panel, the upper row is for beam 1, middle for beam 2 and bottom for beam 3. Black and red dots are the binned matchup averages. Black and red curves are the three-term cosine series fit for VV and HH, respectively.

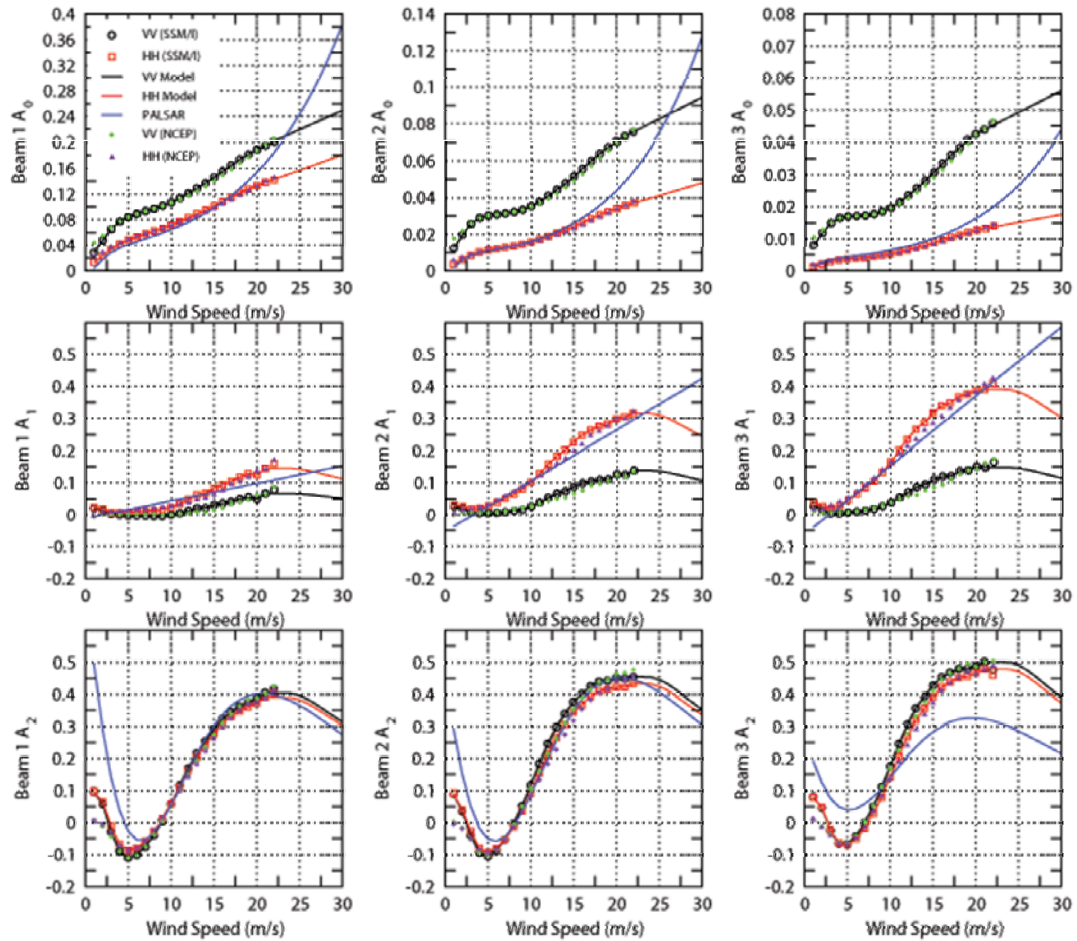


Figure 9.2 The Aquarius radar modeling coefficients ( $A_n$ ) vs. wind speed. The left column is for beam 1, middle for beam 2 and right for beam 3. Black circles and red squares are for the VV and HH matchups with the SSM/I wind speed, respectively. Green diamonds and orange triangles are for the matchups with the NCEP wind speed. The solid black and red curves are the piecewise linear interpolations of the matchups with the SSM/I wind speed. The blue curves correspond to the PALSAR HH GMF.

## 10 Scatterometer Wind Retrieval

---

Retrieves wind speed given the top-of-atmosphere (TOA) NRCS for HH and VV polarization, the KPC values for HH and VV polarization, the NCEP wind direction, the cell azimuth angle and cell incidence angle. We use a maximum likelihood method to determine the wind speed that best agrees with the measured NRCS given the model function and observation geometry. The objective function is:

$$J_w = -\frac{(\sigma_0^{hh} - \sigma_m^{hh})^2}{(\sigma_0^{hh} kp^{hh})^2} - \frac{(\sigma_0^{vv} - \sigma_m^{vv})^2}{(\sigma_0^{vv} kp^{vv})^2}, \quad (10.1)$$

where  $\sigma_0^{hh}$ ,  $\sigma_0^{vv}$  are the TOA NRCS for HH and VV polarization,  $\sigma_m^{hh}$ ,  $\sigma_m^{vv}$  are the model function NRCS which is a function of wind speed, relative azimuth angle, and incidence angle, and the  $kp^{hh}$  and  $kp^{vv}$  are the KPC for HH and VV polarization.

In Fig. 10.1, we plot the Aquarius model function as a function of the relative azimuth angle and wind speed. As shown in the figure, the Aquarius model function is not always monotonic in speed, for a given azimuth and incidence angle, so we must allow for ambiguous wind speeds. To identify multiple solutions in speed, we compute J for every 1 m/s in wind speed, then we find all local minima of J in this coarse search. Around each coarse local minima, we perform a fine search with a 0.1 m/s spacing. If there are multiple solutions, we report the solution that has the nearest speed to NCEP as the retrieved wind speed.

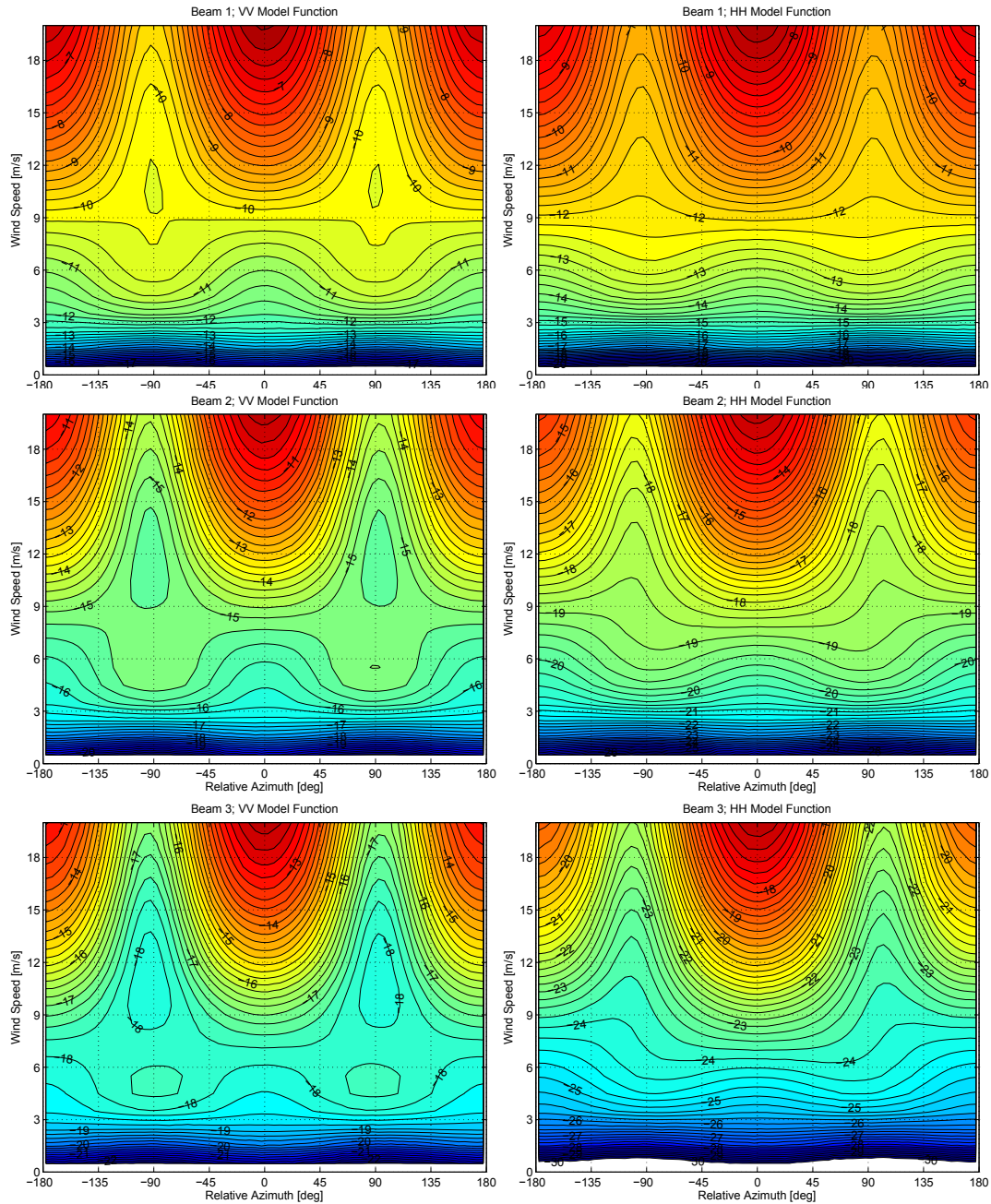


Figure 10.1 Contour plots of Aquarius Model function for the 3 beams at HH and VV polarization. Notice that VV polarization contains closed contours for all 3 beams, indicating a local extrema of the model function. The model function may not be monotonic in the speed dimension for a given relative azimuth angle. Both HH and VV polarizations for all beams show a change in sign of the along-wind / crosswind directional modulation around 7-9 meters / second.

## **11 Acknowledgment**

---

The work described in this paper was carried out by the Jet Propulsion Laboratory, California Institute of Technology under a contract with the National Aeronautics and Space Administration.

## 12 References and Citations

---

- [1] Lagerloef, G., F. R. Colomb, D. Le Vine, F. Wentz, S. Yueh, C. Ruf, J. Lilly, J. Gunn, Y. Chao, A. deCharon, G. Feldman, C. Swift, “The Aquarius/Sac-D Mission: Designed To Meet The Salinity Remote-Sensing Challenge,” *Oceanography*, Vol. 21, no. 1, Special Issue: Sp. Iss. SI, pp. 68-81, Mar 2008.
- [2] D.M. Le Vine, G.S.E. Lagerloef, R. Coloma, S. Yueh, and F. Pellerano, “Aquarius: An Instrument to Monitor Sea Surface Salinity from Space,” *IEEE Trans. Geosci. And Remote Sensing*, Vol. 45, No. 7, 2040-2050, July 2007.
- [3] R.S. Dunbar et al. Science Algorithm Specification for SeaWinds on QuikSCAT and SeaWinds on ADEOS-II. Jet Propulsion Laboratory. 4800 Oak Grove Drive, Pasadena, CA 91109, 2001.
- [4] A. Freedman. Aquarius Instrument Requirements Document (aq-325-0112), April 2009.
- [5] Aquarius Time Tag, Orbit and Attitude Handling for Simulation and Level-1A Data Processing, September 28<sup>th</sup> 2011.
- [6]  $\mathbf{l}=[l_x, l_y, l_z]^T$  is a unit vector that gives the antenna beam bore-sight direction.
- [7] Stefan Schaer and Werner Gurtner. “IONEX: The IONosphere Map EXchange Format Version 1”. In: Astronomical Institute, University of Berne, Switzerland. stefan.schaer@aiub.unibe.ch, 1998.
- [8] International Association of Geomagnetism et al. “International Geomagnetic Reference Field: the eleventh generation”. In: *Geophysical Journal International* 183.3 (2010), pp. 1216–1230. issn: 1365- 246X. doi: [10.1111/j.1365-246X.2010.04804.x](https://doi.org/10.1111/j.1365-246X.2010.04804.x).
- [9] E.J.M. Rignot. “Effect of Faraday rotation on L-band interferometric and polarimetric synthetic- aperture radar data”. In: *Geoscience and Remote Sensing, IEEE Transactions on* 38.1 (2000), pp. 383 –390. issn: 0196-2892. doi: [10.1109/36.823934](https://doi.org/10.1109/36.823934).
- [10] A. Freeman and S.S. Saatchi. “On the detection of Faraday rotation in linearly polarized L-band SAR backscatter signatures”. In: *Geoscience and Remote Sensing, IEEE Transactions on* 42.8 (2004), pp. 1607–1616. issn: 0196-2892. doi: [10.1109/TGRS.2004.830163](https://doi.org/10.1109/TGRS.2004.830163).
- [11] P.A. Wright et al. “Faraday rotation effects on L-band spaceborne SAR data”. In: *Geoscience and Remote Sensing, IEEE Transactions on* 41.12 (2003), pp. 2735–2744. issn: 0196-2892. doi: [10.1109/TGRS.2003.815399](https://doi.org/10.1109/TGRS.2003.815399).
- [12] Michael W. Spencer. “Systematic Errors in the Correction of Faraday Rotation for Aquarius Linearly Polarized Backscatter Measurements”. 334G.2005.02 (rev. A). 2005.
- [13] Dong C. Liu and Jorge Nocedal. “On the limited memory BFGS method for large scale optimization”. In: *Mathematical Programming* 45.1 (Aug. 1989), pp. 503–528. url: <http://dx.doi.org/10.1007/BF01589116>.
- [14] [http://oceancolor.gsfc.nasa.gov/DOCS/ODPS\\_Land\\_Mask.pdf](http://oceancolor.gsfc.nasa.gov/DOCS/ODPS_Land_Mask.pdf)
- [15] Simon H. Yueh, Steve Dinardo, Alexander Fore, and Fuk Li, “Passive and Active L-Band Microwave Observations and Modeling of Ocean Surface Winds”, *IEEE Trans. Geosci. And Remote Sensing*, Vol. 48, No. 8, pp. 3087-3100, August 2010.
- [16] Osamu Isoguchi and Masanobu Shimada, “An L-band Ocean Geophysical Model Function Derived from PALSAR,” *IEEE Trans. Geoscience and Remote Sensing*, Vol. 47, No. 7, pp. 1925-1936, July 2009.
- [17] Kraus, John D., *Radio Astronomy*, 2nd. ed., 1986, Cygnus-Quasar Books, Powell, Ohio.

- [18] Yueh, S. H., "Estimates Of Faraday Rotation With Passive Microwave Polarimetry For Microwave Remote Sensing Of Earth Surfaces," *IEEE Trans. Geosci. Remote Sensing*, Vol. 38, No. 5, 2434-2438, September 2000.
- [19] International GNSS Service TEC products, <http://igsceb.jpl.nasa.gov/components/prods.html>
- [20] C. C. Finlay, S. Maus, C. D. Beggan, T. N. Bondar, A. Chambodut, T. A. Chernova, A. Chulliat, V. P. Golovkov, B. Hamilton, M. Hamoudi, R. Holme, G. Hulot, W. Kuang, B. Langlais, V. Lesur, F. J. Lowes, H. Lühr, S. Macmillan, M. Manda, S. McLean, C. Manoj, M. Menvielle, I. Michaelis, N. Olsen, J. Rauberg, M. Rother, T. J. Sabaka, A. Tangborn, L. Tøffner-Clausen, E. Thébault, A. W. P. Thomson, I. Wardinski, Z. Wei and T. I. Zvereva, "International Geomagnetic Reference Field: the eleventh generation," *Geophys. J. Int.*, 183, pp. 1216–1230, 2010.
- [21] Thomas Meissner and Frank Wentz, The Complex Dielectric Constant of Pure and Sea Water From Microwave Satellite Observations, *IEEE TGARS*, vol. 42 (9), 2004, 1836 – 1849.